

Article

Effects of Support Friction on Mixed-Mode I/II Fracture Behavior of Compacted Clay Using Notched Deep Beam Specimens under Symmetric Fixed Support

Shiyuan Huang^{1,2,3}, Xudong Li³, Wenbing Yu^{1,2}, Xiaofeng Zhang³ and Hongbo Du^{3,*}

¹ State Key Laboratory of Mountain Bridge and Tunnel Engineering, Chongqing Jiaotong University, Chongqing 400074, China; cqjtdxhsy@cqjtu.edu.cn (S.H.)

² School of Civil Engineering, Chongqing Jiaotong University, Chongqing 400074, China

³ Engineering Research Center of Diagnosis Technology and Instruments of Hydro-Construction, Chongqing Jiaotong University, Chongqing 400074, China

* Correspondence: duhongbo@cqjtu.edu.cn

Abstract: This paper investigates the effects of support friction on mixed-mode I/II fracture behavior of compacted clay using notched deep beam (NDB) specimens under symmetric fixed support. Numerical models of 330 NDB specimens were established considering the crack inclination angle, crack length, support span, and support friction coefficient, and the normalized fracture parameters (Y_I , Y_{II} , and T^*) of NDB specimens were calibrated. The numerical results showed that the values of Y_I , Y_{II} , and T^* decreased at different degrees after considering the support friction. Notably, the support friction coefficient could significantly change the loading pattern at the crack tip. To verify this phenomenon, 12 compacted clay NDB specimens were prepared, and a mixed-mode I/II fracture test was performed under fixed support conditions; the phenomenon of asymmetric crack propagation was studied. The test data were processed using the numerical calibration results of Y_I , Y_{II} , and T^* with and without consideration of friction. Afterward, the test data were compared and analyzed by combining the generalized maximum tangential stress (GMTS) and the maximum tangential stress (MTS) criteria. The analysis indicated that the real fracture characteristics of compacted clay NDB specimens could not be reflected when conducting mixed-mode I/II fracture tests under symmetric fixed support conditions if the test results were analyzed by Y_I , Y_{II} , and T^* without considering support friction, as in previous studies.

Keywords: compacted clay; mixed-mode I/II fracture; fracture toughness; notched deep beam; support friction



Citation: Huang, S.; Li, X.; Yu, W.; Zhang, X.; Du, H. Effects of Support Friction on Mixed-Mode I/II Fracture Behavior of Compacted Clay Using Notched Deep Beam Specimens under Symmetric Fixed Support. *Symmetry* **2023**, *15*, 1290. <https://doi.org/10.3390/sym15061290>

Academic Editor: Sergei Alexandrov

Received: 11 May 2023

Revised: 14 June 2023

Accepted: 15 June 2023

Published: 20 June 2023



Copyright: © 2023 by the authors. Licensee MDPI, Basel, Switzerland. This article is an open access article distributed under the terms and conditions of the Creative Commons Attribution (CC BY) license (<https://creativecommons.org/licenses/by/4.0/>).

1. Introduction

Cracks are a common hazard and one of the main causes of damage to all types of geotechnical structures [1,2]. For rockfill dams with clay core walls in water conservancy projects, cracks are a significant threat to the safety of the dam [3]. Due to the difference in the deformation modulus between the clay of the core wall and the stone material of the dam shell, the clay core wall can easily produce transverse or longitudinal cracks because of uneven deformation and dry shrinkage. Under complex stress conditions, the core wall cracks are at risk of further cracking, resulting in the hydraulic splitting of the core wall and threatening the safety of the dam [4].

Since Skempton et al. [5] suggested explaining the destabilization process of fracture-containing hard clay slopes using the fracture mechanics theory, more studies have been conducted on the fracture properties of clay materials. In terms of mode I fracture properties, Lakshminantha et al. [6] and Lee et al. [7] investigated the mode I fracture toughness of compacted clay using compact tension (CT) specimens. CT specimens were inspired by a method recommended by the American Society for Testing and Materials (ASTM) [8] for

metallic materials, which required holes to be drilled in the specimen for fixture attachment. The specimen preparation and test preparation were complicated, and the fracture was likely to occur at the fixture due to the low tensile strength of the clay material. Zhang et al. [9] followed the idea of direct tensile loading, and uniaxial tensile tests were conducted using unilateral open-joint rectangular clay specimens. The test operation was relatively simple, but it was easy to fracture at the end of the specimen when using epoxy vinyl to bond the end of the specimen. For compacted clay, the bending loading method is more convenient and widely used. Most scholars used single-edge notched beam (SENB) specimens [10–14] recommended by the ASTM [8] to carry out mode I fracture tests of compacted clay. Some scholars used semi-circular bend (SCB) specimens [15,16] recommended by the ISRM [17] to test the mode I fracture toughness of compacted clay. However, the mode I/II fracture properties of the clay were barely studied. Only Wang et al. [18] used a four-point bending method to perform a mixed-mode I/II fracture test on the SENB specimens of compacted clay. Aliha et al. [19] investigated the mixed-mode I/II fracture properties of air-dried compacted clay using asymmetric semi-circular bend (ASCB) specimens [20]. Since most cracks in the core walls of rockfill dams are under mixed stress, studying the mixed-mode I/II fracture in compacted clay is of great engineering importance [21,22].

Considering the convenience of preparing fracture specimens of compacted clay, scholars usually use non-circular SENB specimens for clay fracture tests. However, there is a large length-to-width ratio (greater than 4.5) for the SENB specimens recommended by the ASTM [8]. For compacted clay with low tensile strength, slight disturbance during the demolding and transfer of the specimen may damage the SENB specimen of the compacted clay [12,16]. The single-sided notched deep beam (NDB) specimen (i.e., SENB specimen with a length-to-width ratio of 2:1) proposed by Luo et al. [23] can effectively reduce the clay specimen disturbance before the test and save the test material [24].

In the past decades, researchers employed the three mentioned support types of I, II, and III for conducting three-point bending fracture tests on different materials and test specimens. According to Bahrami et al. [25], the types of support for loading in bending tests can be classified into three categories (type I, II, and III): roller support, roller in groove, and fixed support, respectively. The impact of supports on the fracture results has often not been considered, and there is very little research in the literature studying the effect of support friction. In recent years, some scholars have found that the supports used in three-point bending fracture tests can affect the cracking behavior of materials significantly. Bahrami et al. [25,26] investigated the effect of support type on the fracture toughness of polymethyl methacrylate and rock materials in SCB tests. Qin et al. [27] investigated the influence of friction on the determination of rock mode I fracture toughness using an SCB specimen. Pirmohammad et al. [28,29] discussed the effect of support type on the fracture toughness of asphalt concrete using SCB specimen at various temperatures. Bakhshizadeh et al. [30] provided an investigation of the impact of support type on the fracture mode of loading using an SCB specimen. Ayatollahi et al. [31] evaluated the effects of support friction on the mode I stress intensity factor and the fracture toughness values determined from SENB testing. It should be noted that the mentioned investigations have been considered under pure mode I and pure mode II, and no studies have been carried out so far concerning the effect of supports on mixed mode I/II fracture behavior in NDB tests.

Among the three mentioned support types, only type I has no friction between the support and the specimen [31]. However, this type of support is disadvantaged by the inconvenient fixation for clay fracture specimens with small peak loads [16], thus the fixed support was mostly used in previous clay fracture tests. The fracture parameters derived using the normalized stress intensity factor (SIF) without considering the support friction cannot reflect the real fracture properties of compacted clay [32].

Therefore, the current study considers the impact of support friction on the mixed mode I/II fracture behavior of compacted clay using the NDB specimen under symmetric fixed support. First, the frictional effect between the support and the specimen was considered, and the normalized K_I , K_{II} , and T -stress at the crack tip of the NDB specimen

were numerically calibrated using the finite element method. Their variation in the crack inclination angle under different support friction coefficients was analyzed, demonstrating the effect of the support friction coefficient on the normalized K_I , K_{II} , and T -stress. Then, the mixed-mode I/II fracture test was performed on compacted clay using NDB specimens. The differences in the fracture properties of the compacted clay, with and without the consideration of support friction, were analyzed. With the generalized maximum tangential stress (GMTS) criterion [33], the differences between the mixed-mode I/II fracture properties of compacted clay under the two conditions and the theoretical values were discussed.

2. Numerical Model for NDB Specimens

2.1. Loading Principle of NDB Specimens

The elastic stress field at the crack tip can be expressed as a set of expansions of an infinite series, as shown in Equation (1) [34]:

$$\begin{cases} \sigma_\theta = \frac{1}{\sqrt{2\pi r}} \cos \frac{\theta}{2} \left(K_I \cos^2 \frac{\theta}{2} - \frac{3}{2} K_{II} \sin \theta \right) + T \sin^2 \theta + O(r^{1/2}) \\ \sigma_r = \frac{1}{\sqrt{2\pi r}} \cos \frac{\theta}{2} \left[K_I \left(1 + \sin^2 \frac{\theta}{2} \right) + K_{II} \left(\frac{3}{2} \sin \theta - 2 \tan \frac{\theta}{2} \right) \right] + T \cos^2 \theta + O(r^{1/2}) \\ \tau_{r\theta} = \frac{1}{2\sqrt{2\pi r}} \cos \frac{\theta}{2} \left[K_I \sin \theta + K_{II} (3 \cos \theta - 1) \right] - T \sin \theta \cos \theta + O(r^{1/2}) \end{cases} \quad (1)$$

where r and θ are the crack tip coordinates; the first term is the singular term (the $r^{-0.5}$ term); the second term is the non-singular term (the r^0 term); and $O(r^{1/2})$ is the higher-order term, which is usually not considered because $O(r^{1/2})$ is much smaller than the first two terms.

The SIF can reflect the strength of the stress field around the crack tip. Although the non-singular stress term (T -stress) is relatively small, it has a certain influence on the initiation and development of the crack [33,35]. Therefore, the SIFs, K_I , K_{II} , and T -stress, are important parameters for studying mixed-mode I/II fracture problems.

As shown in Figure 1, for the NDB specimen proposed by Luo et al. [23], the specimen width is W , the specimen length is $2W$, the crack length is a , the angle between the pre-fabricated crack and the loading direction is β , the support span is $2S$, and the specimen thickness is B .

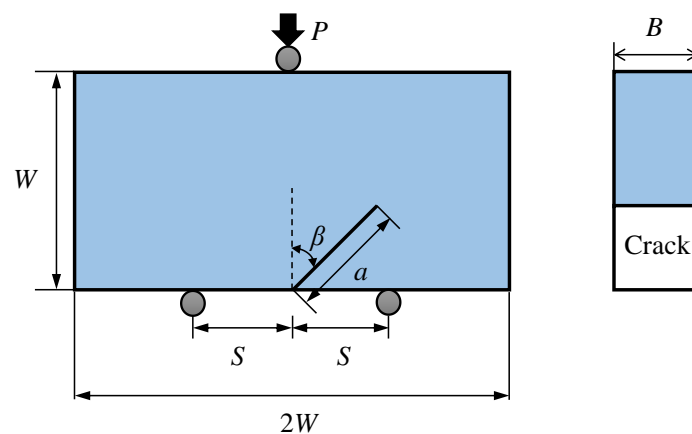


Figure 1. Schematic view of the NDB specimen and its related parameters.

The K_I , K_{II} , and T -stress at the crack tip of the NDB specimen can be expressed as:

$$K_I = \frac{P\sqrt{\pi a}}{2WB} Y_I \quad (2)$$

$$K_{II} = \frac{P\sqrt{\pi a}}{2WB} Y_{II} \quad (3)$$

$$T = \frac{P}{2WB} T^* \quad (4)$$

where Y_I , Y_{II} , and T^* are normalized factors of the mode I SIF, mode II SIF, and T -stress, respectively, and P is the applied load.

For the loading modes of the crack in the NDB specimen, when the crack inclination angle β of the NDB specimen is 0, $K_I \neq 0$, $K_{II} = 0$, the crack is subjected to pure mode I loading. As the crack dip angle β gradually increases, the crack loading condition can be changed from the pure mode I to mixed mode I/II ($K_I \neq 0$, $K_{II} \neq 0$), and pure mode II loading ($K_I = 0$, $K_{II} \neq 0$) is obtained when the crack dip angle β reaches a specific degree.

2.2. Finite Element Model of NDB Specimens

In previous studies, the fracture stress field calibration of fracture specimens usually excluded the support friction effect, and the normalized factors Y_I , Y_{II} , and T^* were only functions influenced by β , a/W , and S/W . After considering the support friction, the normalized factors Y_I , Y_{II} , and T^* became functions influenced by β , a/W , S/W , and f . Therefore, quantifying the effect of support friction on the stress field at the crack tip of NDB specimens is essential for accurately determining the fracture properties of the test material.

In this study, the finite element software ABAQUS was used to establish the numerical model for NDB specimens. As shown in Figure 2, the NDB specimen has a length of $2W = 75$ mm, a width of $W = 37.5$ mm, a thickness of $B = 30$ mm thick, and an applied reference load of $P = 1000$ N. According to previous studies, the modulus of elasticity and Poisson's ratio have no effect on the calibration of the stress field [36]. Therefore, the modulus of elasticity and Poisson's ratio were taken as 1.65 GPa and 0.35, respectively.

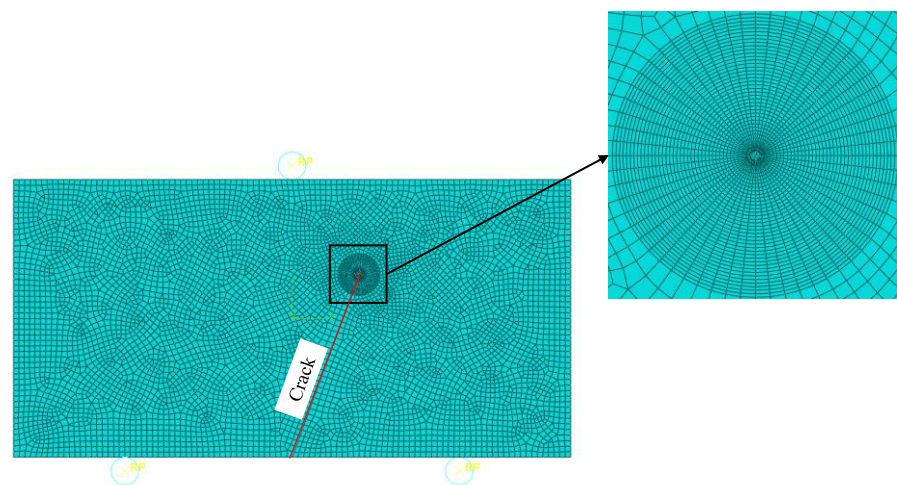


Figure 2. Finite element model of the NDB specimen.

To simulate the boundary conditions of the NDB specimen, the support at the bottom was completely fixed, and the loading point at the top was limited to moving in the vertical direction only. The entire specimen was loaded by applying a vertical downward concentrated force to the top loading point. To reflect the friction coefficient between the actual support point and the specimen, a discrete rigid body was used to model the top loading point and the bottom support [25,31], each of the three supports was modeled as a rigid part, and the frictional contact was regarded between the supports and the specimen. The mesh division model of the NDB specimen at $\beta = 20^\circ$, $a/W = 0.6$, and $S/W = 0.6$ is illustrated in Figure 2.

The J -integral approach was adopted to calculate K_I and K_{II} , and the integral interaction method was used to calculate T -stress [23,24,30]. Due to the singularity of stress distribution near the crack tip, singular cells were arranged in the first ring of the crack tip, and the size of the singular cells was less than $1/100$ of the crack length a . In addition, a

20-turn four-node quadratic integral quadrilateral cell was divided around the singular cell using a sweeping technique. The distance between the edge of the outermost ring cell and the crack tip was about 1/9 of the crack length, and the rest of the region was divided freely to produce quadrilateral cells. The K_I , K_{II} , and T -stress at the crack tip of the specimen can be obtained by numerical computation. Then, Y_I , Y_{II} , and T^* can be back-calculated according to Equations (2)–(4).

In order to verify the reasonableness of the model, the crack tip stress field of the NDB specimen at $f = 0$ and $a/W = 0.4$ was calculated and compared with the results of Luo et al. [23], as shown in Figure 3. With a different S/W and different β , the Y_I obtained through numerical simulation is basically consistent with the Y_I patterns and magnitudes obtained from the literature [23], demonstrating the rationality of the proposed numerical model.

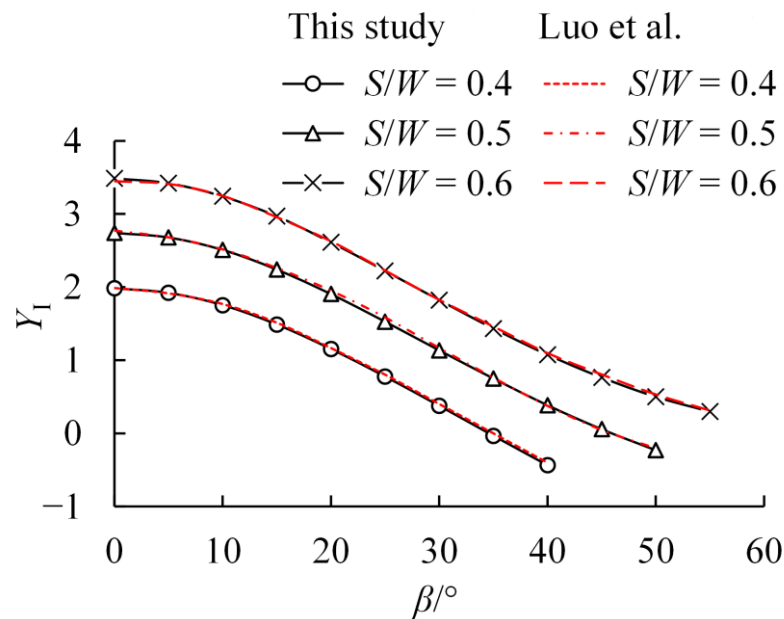


Figure 3. Validation of the proposed numerical model, Luo et al. [23].

2.3. Calculation Scheme

To investigate the effect of support friction on the crack tip stress field of NDB specimens, the effect of the support friction coefficient f was added based on the conventional calibration work considering β , a/W , and S/W . The calculation scheme is shown in Table 1, with 2 S/W , 3 a/W , 5 f , 11 β , and 330 models selected.

Table 1. Calculation scheme.

S/W	a/W	f	$\beta/^\circ$
0.6	0.4, 0.5, 0.6	0, 0.2, 0.4, 0.6, 0.8	0, 5, 10, 15, 20, 25, 30, 35, 40, 45, 50
0.8	0.4, 0.5, 0.6	0, 0.2, 0.4, 0.6, 0.8	0, 5, 10, 15, 20, 25, 30, 35, 40, 45, 50

3. Effect of Support Friction on the Stress Field at the Crack Tip of NDB Specimens

3.1. Variation Curve of Y_I with β under Different Support Friction Conditions

Through the calculation of 330 numerical models, the K_I , K_{II} , and T -stress at the crack tip in each model were obtained. Then, the Y_I , Y_{II} , and T^* values were obtained by back-calculating according to Equations (2)–(4).

As shown in Figure 4, Y_I gradually decreases with increasing β for any a/W , S/W , and f condition. When a/W and S/W are fixed, the slope of the Y_I - β curve gradually decreases

with the increase in the friction coefficient f , and the influence of support friction on Y_I is more significant when β is small.

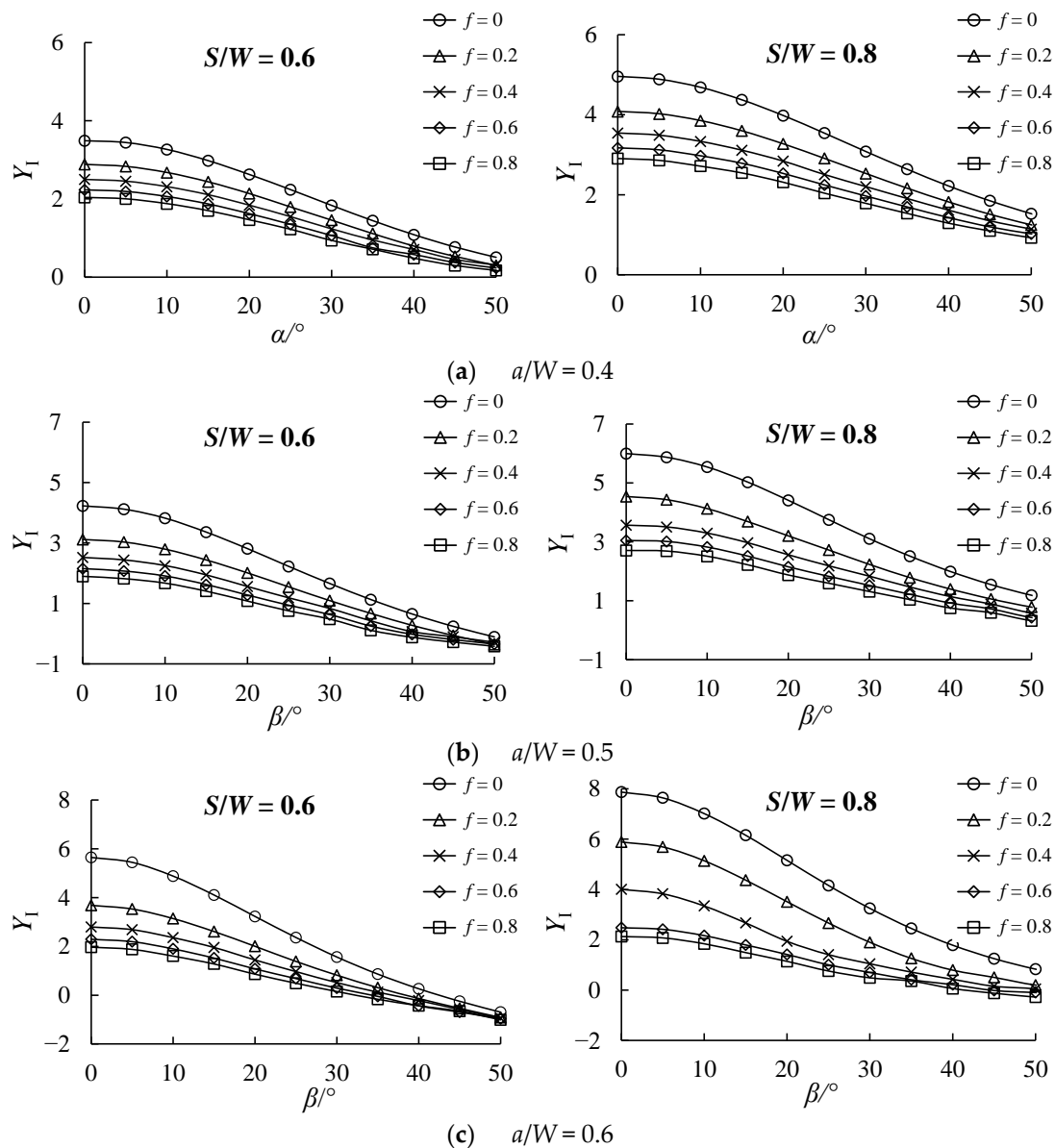


Figure 4. Variation curves of Y_I with β under different a/W , S/W , and f conditions, (a) $a/W = 0.4$, (b) $a/W = 0.5$, (c) $a/W = 0.6$.

The comparison of the Y_I - β curves under different S/W conditions suggests that when a/W is fixed, a larger S/W leads to a larger Y_I , which is more sensitive to the influence of support friction. Comparing the Y_I - β curves under different a/W conditions, it can be concluded that when S/W is fixed, a larger a/W leads to a larger Y_I , which is more significantly affected by the support friction.

In addition, there is a critical dip angle β_{II} of the crack in a certain range between a/W and S/W . It makes $Y_I = 0$, indicating that the crack achieves pure mode II loading. However, at a large S/W and small a/W , pure mode II loading of cracks cannot be achieved, no matter how much β increases.

Interestingly, the critical crack inclination angle β_{II} corresponding to the pure mode II loading condition ($Y_I = 0$) of the NDB specimen changed significantly after considering the support friction, indicating that the support friction significantly impacts the loading state of the crack, which directly affects the scheme design of the mixed-mode I/II fracture test.

3.2. Variation Curve of Y_{II} with β under Different Support Friction Conditions

As shown in Figure 5, under any a/W , S/W , and f condition, as the crack inclination angle β increases, mode II load components start to appear, Y_{II} increases first and then decreases, and the Y_{II} - β relation curve is distributed in an asymmetric parabolic pattern.

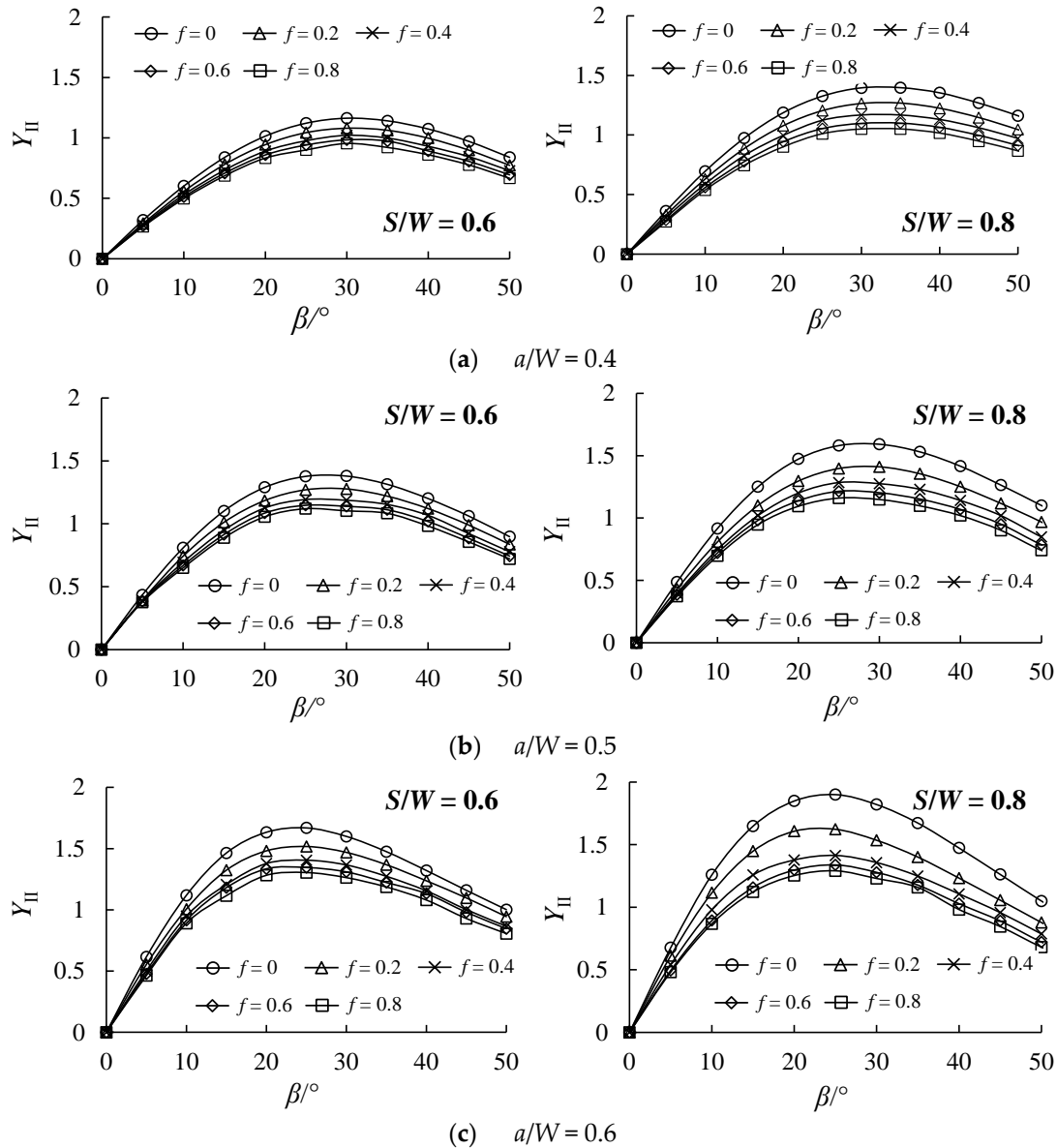


Figure 5. Variation curves of Y_{II} with β under different a/W , S/W , and f conditions. (a) $a/W = 0.4$; (b) $a/W = 0.5$; (c) $a/W = 0.6$.

Overall, when a/W and S/W are certain, increasing f only decreases Y_{II} , but does not affect the trend of Y_{II} - β curve, and the β corresponding to the maximum Y_{II} is also basically unchanged. In addition, as S/W or a/W increases, Y_{II} increases gradually, and it is more sensitive to the influence of support friction.

As seen in Figure 4, Y_I corresponding to the β that maximizes Y_{II} is not 0, which indicates that the Y_{II} of the crack is not the maximum value during pure mode II loading.

3.3. Variation Curve of T^* with β under Different Support Friction Conditions

Extensive literature has shown that T -stress has a non-negligible role in crack initiation and expansion [20,37–40]. Therefore, the normalized T -stress (T^*) of NDB specimens was calibrated in this paper.

As seen in Figure 6, T^* gradually increases with increasing β , and then stabilizes or slightly decreases. Its value reveals that the T -stress gradually changes from compressive to tensile stress. As a/W increases, the $Y_{II} \sim T^*$ curve changes gradually from an approximately linear to a convex S-shaped curve, and the β corresponding to the maximum T^* decreases gradually.

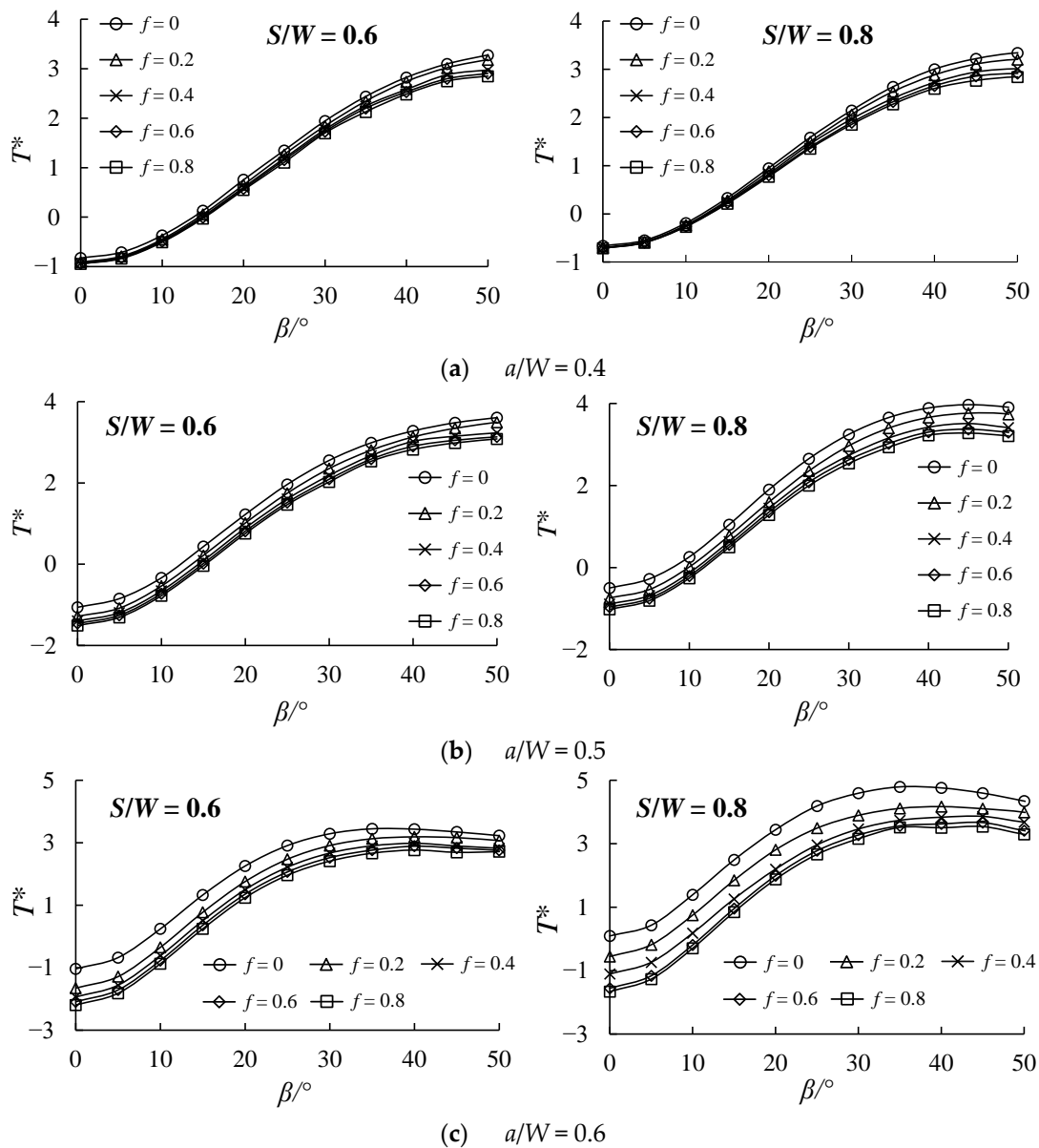


Figure 6. Variation curve of T^* with β under different a/W , S/W , and f conditions. (a) $a/W = 0.4$; (b) $a/W = 0.5$; (c) $a/W = 0.6$.

Similar to the rule in Figures 4 and 5, T^* is more significantly influenced by the support friction at a larger S/W or larger a/W .

3.4. Effect of Support Friction on Y_I

To further observe the influence law of the support friction coefficient on Y_I , the $Y_I \sim f$ relation curve was drawn, as shown in Figure 7. Under different a/W , S/W , and β conditions, Y_I decreases gradually with the increase in f ; when f increases to a certain extent, it basically has no effect on Y_I . This result is because the load P acting on the specimen is fixed in numerical calibration. As f increases, the friction between the support

and the specimen increases, and the load that causes the specimen to fracture gradually decreases, thus decreasing K_I and Y_I .

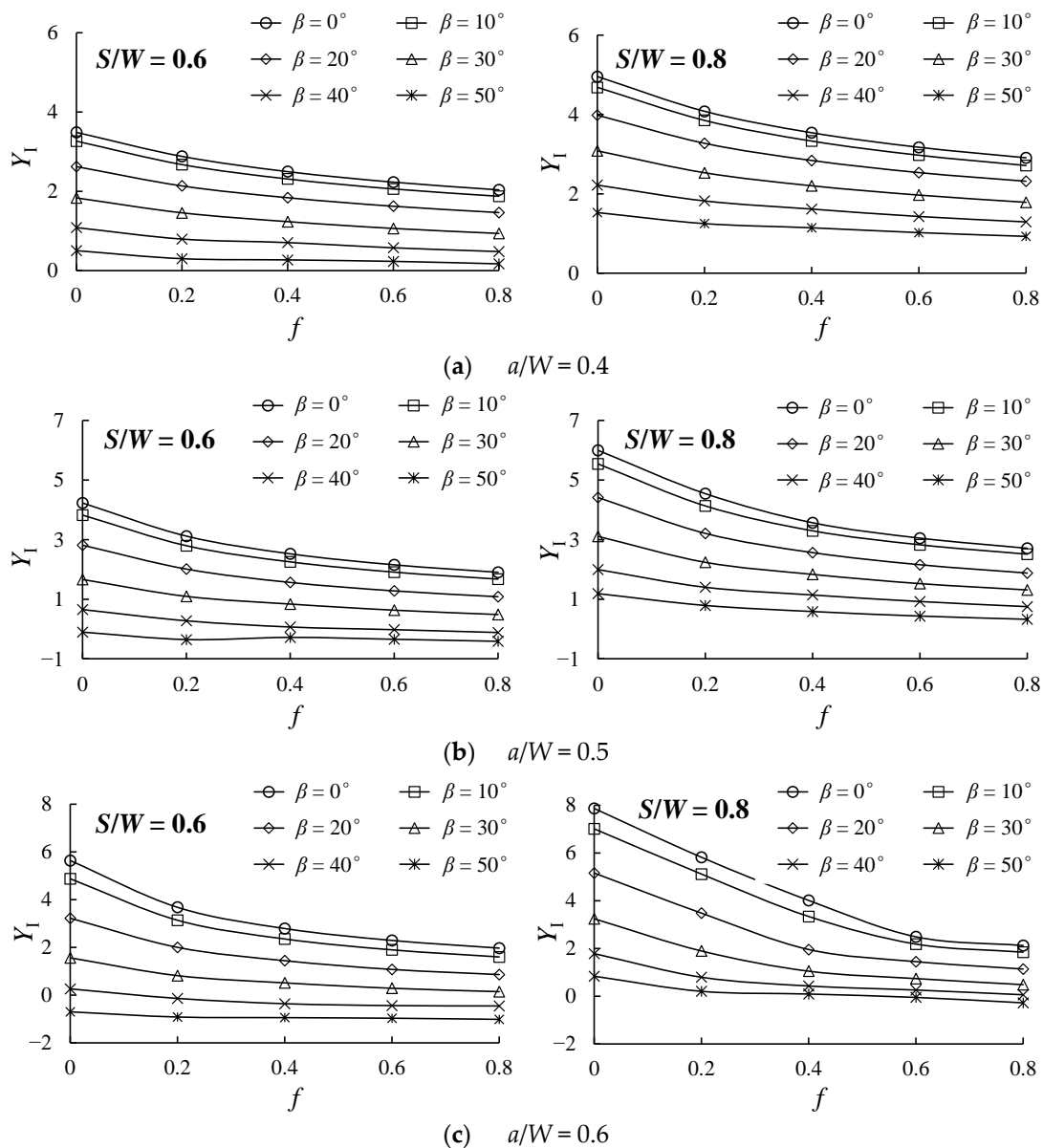


Figure 7. Variation curve of Y_I with f under different a/W , S/W , and β conditions. (a) $a/W = 0.4$; (b) $a/W = 0.5$; (c) $a/W = 0.6$.

3.5. Effect of Support Friction on Y_{II}

To further observe the influence law of the support friction coefficient on Y_I , the relation curve of Y_{II} - f under different cases was drawn, as shown in Figure 8. Overall, when other factors are certain, Y_{II} gradually decreases with the increase in f (except for $\beta = 0^\circ$ when Y_{II} is 0, since the crack is the pure mode I loading). Additionally, Y_{II} is more sensitive to support friction when S/W or a/W is larger. By comparing with Figure 7, it can be found that the influence of support friction on Y_I is significantly greater than that on Y_{II} .

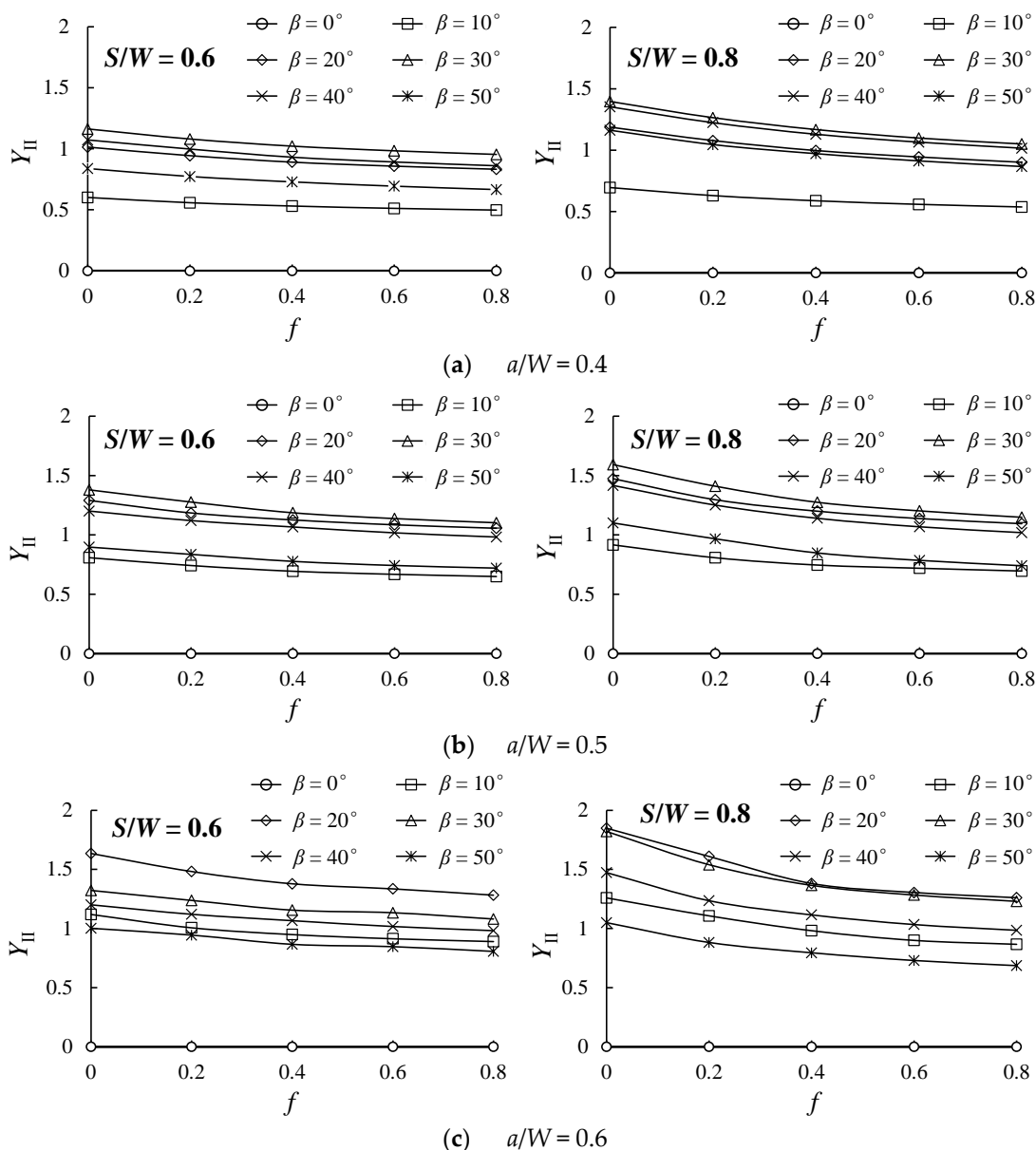


Figure 8. Variation curve of Y_{II} with f under different a/W , S/W , and β conditions. (a) $a/W = 0.4$; (b) $a/W = 0.5$; (c) $a/W = 0.6$.

3.6. Effect of Support Friction on T^*

The T^*-f relation curves for different a/W , S/W , and β conditions are shown in Figure 9. Overall, T^* is not sensitive to f when a/W is small, regardless of the variation of β and S/W , and shows a horizontal trend. As a/W increases, the T^*-f relation curve gradually shows a decreasing trend. For example, when $a/W = 0.6$, T^* gradually decreases as f increases and tends to be stable after f reaches a certain value.

In addition, as a/W increases, the T^*-f curve corresponding to $\beta = 30^\circ$ gradually approaches the T^*-f curve corresponding to $\beta = 40^\circ$ and $\beta = 50^\circ$, which is because increasing a/W leads to a smaller β corresponding to the maximum T^* .

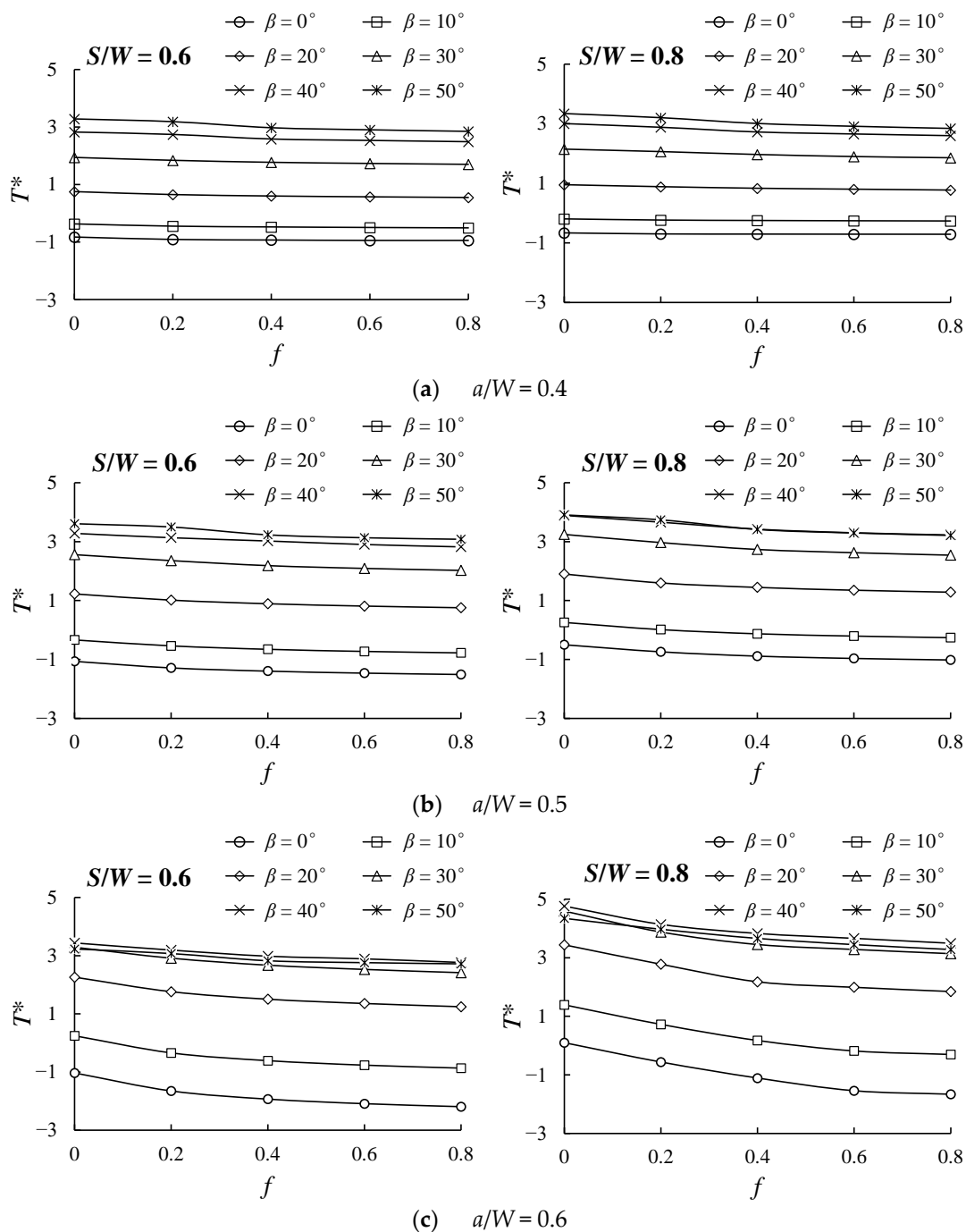


Figure 9. Variation curves of T^* with f under different a/W , S/W , and β conditions. (a) $a/W = 0.4$; (b) $a/W = 0.5$; (c) $a/W = 0.6$.

3.7. Effect of Support Friction on the Pure Mode II Crack Inclination Angle

As seen in Figure 4, the support friction has a significant effect on the normalized mode I SIF at the crack tip of the NDB specimen and directly affects the critical crack inclination angle β_{II} under pure mode II loading. Therefore, the critical crack inclination angle β_{II} of NDB specimens under different a/W , S/W , and f conditions is given according to the calculation scheme in this paper, as shown in Tables 2 and 3.

Table 2. Crack inclination β_{II} of the NDB specimen under pure mode II loading at $S/W = 0.6$.

a/W	$\beta_{II}/(^{\circ})$				
	$f = 0$	$f = 0.2$	$f = 0.4$	$f = 0.6$	$f = 0.8$
0.4	-	-	-	-	-
0.5	49	44	42	40	38
0.6	42	39	37	34	32

Table 3. Crack inclination β_{II} of the NDB specimen under pure mode II loading at $S/W = 0.8$.

a/W	$\beta_{II}/(^{\circ})$				
	$f = 0$	$f = 0.2$	$f = 0.4$	$f = 0.6$	$f = 0.8$
0.4	-	-	-	-	-
0.5	-	-	-	-	-
0.6	-	57	51	45	42

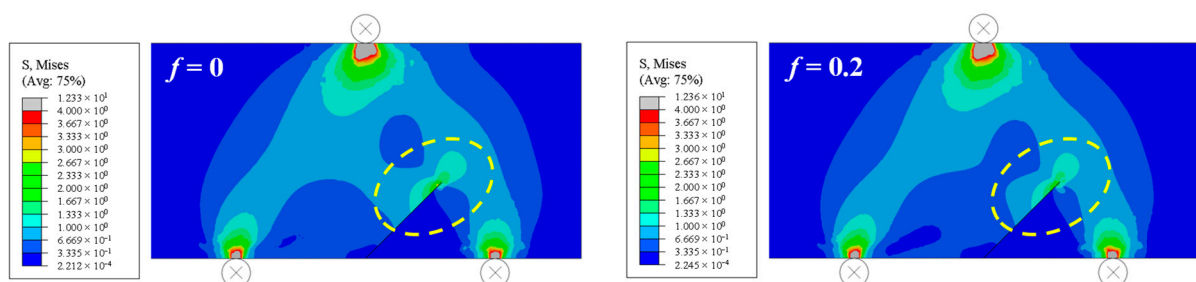
From Table 2, it can be concluded that the crack cannot achieve pure mode II loading at $S/W = 0.6$ and $a/W = 0.4$. When $S/W = 0.6$, and $a/W = 0.5$ and 0.6 , the crack can achieve pure mode II loading in the range of $f = 0$ – 0.8 , and the critical crack inclination angle β_{II} gradually decreases as f increases.

From Table 3, it can be deduced that the crack cannot achieve pure mode II loading at $S/W = 0.8$, and $a/W = 0.4$ and 0.5 . When $S/W = 0.8$ and $a/W = 0.6$, the critical crack inclination angle β_{II} gradually decreases as f increases. In addition, with the support friction considered, pure mode II loading can be achieved in cases where it cannot be achieved originally, such as the case of $a/W = 0.6$, $S/W = 0.8$, and $f = 0$.

First, it is necessary to reduce the S/W or increase a/W to achieve the full range of the mixed-mode I/II fracture test for cracks from pure mode I to pure mode II based on the three-point bending test of NDB specimens, and reduce the critical inclination angle β_{II} for the convenience of specimen processing. Additionally, it can also be achieved by fixing the support and increasing the roughness of the support.

3.8. Effect of Support Friction on Mises Stress at the Crack Tip

Mises stress nephogram of a typical NDB specimen ($a/W = 0.5$, $S/W = 0.6$, $\beta = 45^{\circ}$) with different friction coefficients is shown in Figure 10. With the increase in the friction coefficient f , the range of Mises stress profile at the crack tip gradually decreases and basically stabilizes after f reaches 0.4 , which confirms the trend of the normalized fracture parameter mentioned above that first decreases and then stabilizes with the increasing friction coefficient (Figures 7–9). In addition, the elliptical zone (i.e., red- and orange-colored zones) near the bottom support tends to rotate inside the specimen due to friction force at the contact points.

**Figure 10.** Cont.

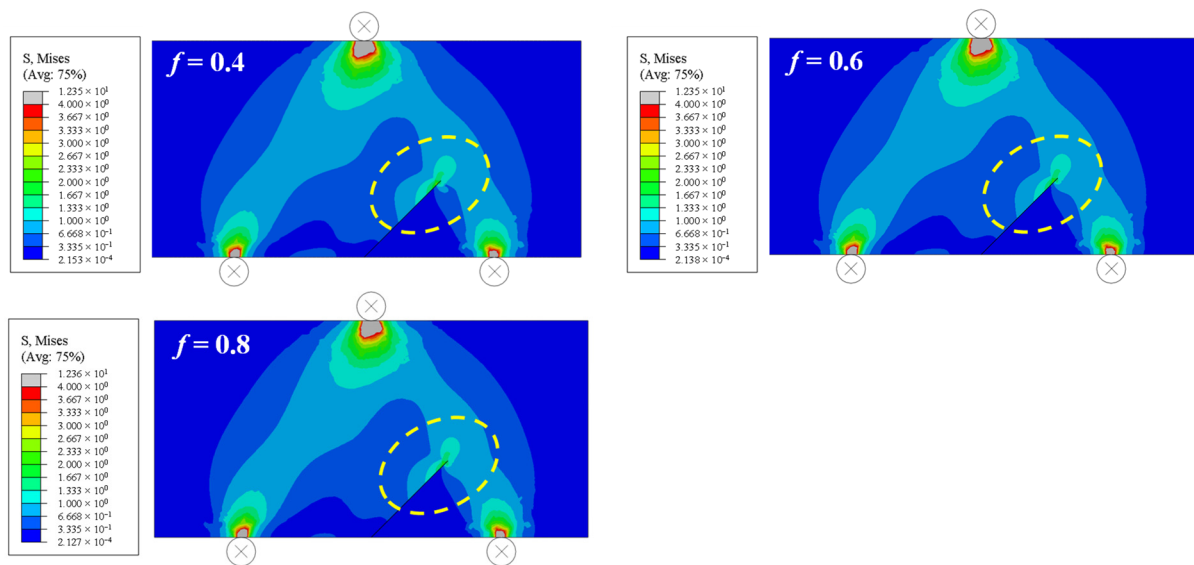


Figure 10. Distribution of Mises stress in the NDB specimen for different values of the friction coefficient.

4. Mixed-Mode I/II Fracture Test of Compacted Clay Using NDB Specimens

4.1. Test Purpose

To investigate the influence of support friction on the mixed-mode I/II fracture behavior of compacted clay using NDB specimens, a mixed-mode I/II fracture test was conducted on compacted clay under symmetric fixed support conditions. The primary objectives of the test are as follows: (1) To evaluate the mixed-mode I/II fracture behavior of compacted clay utilized in this study; (2) To analyze the variation in mixed-mode I/II fracture parameters of compacted clay, with and without support friction; (3) To furnish test data for discussion on fracture criterion analysis.

4.2. Soil Parameters

The test clay was taken from a construction site in Chongqing, China. Its particle size distribution is as follows: 0.5–0.25 mm (0.5%), 0.25–0.1 mm (17.9%), 0.1–0.075 mm (41.6%), and <0.075 mm (40.0%). Its basic physical and mechanical properties are as follows: specific gravity $G_s = 2.72$, plasticity index $I_p = 20.1$, liquid limit $W_L = 50.1\%$, plastic limit $W_P = 30.0\%$, maximum dry density $\rho_{max} = 1.68 \text{ g/cm}^3$, optimal moisture content $w_{op} = 16.6\%$, tensile strength $\sigma_t = 44.3 \text{ kPa}$, cohesion $c = 48.5 \text{ kPa}$, and internal friction angle $\varphi = 16.3^\circ$.

4.3. Specimen Preparation Method and Loading Instrument

The specimen was prepared using a self-made compaction vessel with the dimensions of $100 \times 50 \times 80 \text{ mm}$. First, the dry density and moisture content of the compacted clay specimen were controlled to calculate the required mass of soil and water. In this test, a 95% degree of compaction was selected, the dry density of the compacted clay specimen was 1.6 g/cm^3 , and the optimum moisture content of 16.6% was taken. Then, the soil materials were mixed thoroughly, and the well-mixed soil materials were poured into a fresh-keeping bag in an airtight container to rest for 24 h. Second, the soil materials were poured into the compaction vessel, and rectangular specimens of 100 mm in length, 50 mm in width and 30 mm in thickness were obtained through layered compaction. Finally, the specimens were demolded, and then cutting equipment was used for crack preparation. The specimen preparation process is shown in Figure 11.

During the compaction, the configured soil materials were compacted in three layers. The quality of each layer was controlled as equally as possible, and each layer was fully scraped after compaction [16]. To facilitate the demolding of the specimens, a certain

amount of lubricant was applied to the side walls and bottom of the compaction vessel before pouring in the soil material [16].



Figure 11. Preparation process of specimens. (a) Natural soil; (b) mixing soil; (c) before compacting; (d) after compacting.

All tests for this study were conducted at the Key Laboratory for Hydraulic and Waterway Engineering of the Ministry of Education of Chongqing Jiaotong University. As shown in Figure 12, the self-developed DTV-3 soil fracture instrument was used, including a servo motor, load sensor, displacement sensor, telescopic rod, fixture, and data acquisition software. The maximum axial load and axial displacement were 3 kN and 40 mm, respectively, the precision was 0.1 N, and the loading rate ranged from 0.12 to 30 mm/min. In this NDB tests, displacement-controlled loading was adopted at a rate of 0.8 mm/min [16,41], and the bottom was a fixed steel support.

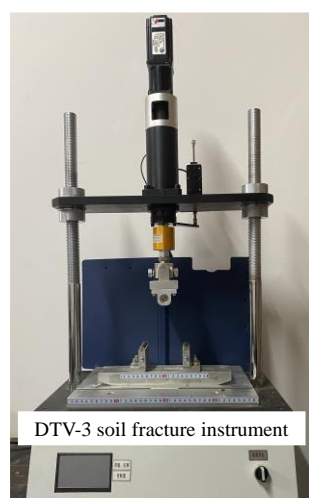


Figure 12. DTV-3 soil fracture instrument.

4.4. Friction Coefficient of the Compacted Clay–Steel Interface

The friction coefficient of the compacted clay–steel interface was determined using the method [41,42] shown in Figure 13. First, the prepared NDB specimen was placed in the middle of the steel plate. Then, the steel plate was slowly raised until the specimen began to slide. The lifting height, h , of the steel plate was tested. The friction coefficient f can be calculated according to the relationship between f and α ($f = \tan\alpha$), where α is the angle between the steel plate and the horizontal direction. According to the above method, the average f was 0.4 for the compacted clay NDB specimen and the steel plate under the steel support (the steel plate is of the same material as the steel support), i.e., the friction coefficient between the support and the specimen was regarded as 0.4 in this paper.

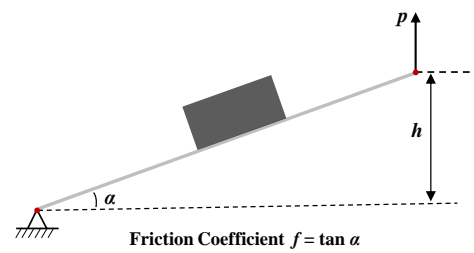


Figure 13. Determination method of the friction coefficient.

4.5. Test Scheme

According to the numerical calibration results in Section 3, NDB specimens with $a/W = 0.6$ and $S/W = 0.6$ (specimen size of 100 mm \times 50 mm \times 30 mm) were selected to perform the mixed-mode I/II fracture test.

To verify the effect of support friction on the test results, consistent with previous studies, support friction was not considered in designing the crack inclination angle of the specimens. According to the Y_I - β curve corresponding to $f = 0$ in Figure 4, six crack inclination angles were selected, namely $\beta = 0^\circ$ (pure mode I), 10° , 20° , 30° , 37° , and 42° (pure mode II). Two sets of parallel specimens, totaling 12 specimens, were considered.

To facilitate the processing and analysis of the test results, the normalized factors Y_I , Y_{II} , and T^* of NDB specimens at $a/W = 0.6$ and $S/W = 0.6$ were compiled according to Figures 4–6, as shown in Figure 14.

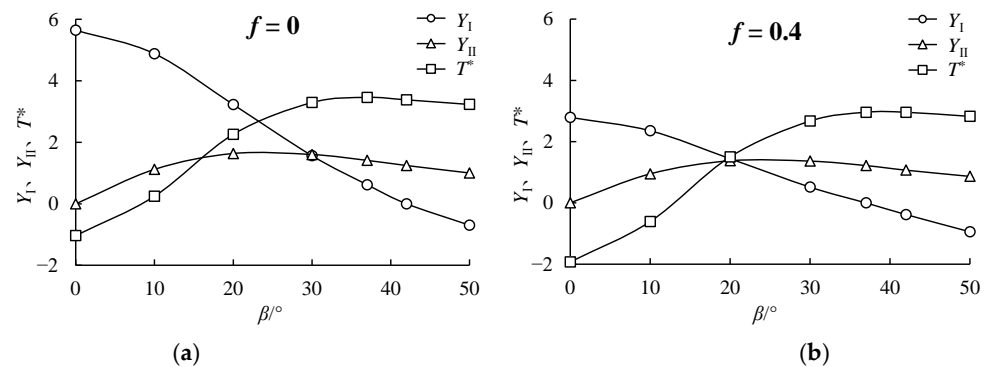


Figure 14. Normalized factors of NDB specimens at $a/W = 0.6$ and $S/W = 0.6$, (a) without considering support friction, and (b) considering support friction.

5. Test Results and Analysis

Figures 4 and 5 show the results of the mixed-mode I/II fracture test of compacted clay without and with consideration of support friction, respectively. As illustrated in the Tables 4 and 5, the combined relationship between K_I and K_{II} is represented by M^e . As shown in Equation (5), $M^e = 0$ corresponds to pure mode II, $M^e = 1$ corresponds to pure mode I, and M^e between 0 and 1 is compound loading.

$$M^e = \frac{2}{\pi} \tan^{-1} \left(\frac{K_I}{K_{II}} \right) \quad (5)$$

As shown in Figure 4, when $\beta = 0^\circ$, K_{II} is 0, the crack is the pure mode I loading and K_{IC} is 19.01 $\text{kPa} \cdot \text{m}^{0.5}$. When $\beta = 42^\circ$, K_I is 0, the crack is pure mode II loading, K_{IIC} is 7.79 $\text{kPa} \cdot \text{m}^{0.5}$, and the fracture toughness ratio K_{IIC}/K_{IC} is 0.41.

As shown in Table 5, the mixed-mode I/II fracture characteristics of compacted clay change significantly after data processing using Y_I , Y_{II} , and T^* , considering support friction.

When $\beta = 0^\circ$, the crack is still under pure mode I loading and K_{IC} is 9.41 $\text{kPa} \cdot \text{m}^{0.5}$; however, the value is 51% lower than the K_{IC} without considering support friction. When $\beta = 42^\circ$, K_I is $-2.31 \text{ kPa} \cdot \text{m}^{0.5}$ and the crack is in the compression-shear-stress state, which

does not belong to mixed-mode I/II fracture. Due to the support friction, the critical inclination angle β_{II} of the crack corresponding to pure mode II becomes smaller. When $\beta = 37^\circ$, K_I is very small, approximately equal to 0, so it is considered to be pure mode II loading at this time. Correspondingly, K_{IIC} is $6.63 \text{ kPa}\cdot\text{m}^{0.5}$, which is 15% lower than K_{IIC} without considering the support friction, and the fracture toughness ratio K_{IIC}/K_{IC} is 0.71, which is 72% higher than K_{IIC}/K_{IC} without considering the support friction. In addition, the M^e corresponding to different β values decreases after considering the support friction, indicating that the support friction increases the proportion of mode II loading at the crack tip of the NDB specimen.

Table 4. Mixed-mode I/II fracture test results of compacted clay without considering support friction.

β ($^\circ$)	M^e	K_I ($\text{kPa}\cdot\text{m}^{0.5}$)	K_{II} ($\text{kPa}\cdot\text{m}^{0.5}$)	K_I/K_{IC}	K_{II}/K_{IC}	T (kPa)
0	1.00	19.01	0.00	1.00	0.00	−13.08
10	0.86	15.57	3.57	0.82	0.19	2.96
20	0.70	11.82	5.98	0.62	0.31	31.12
30	0.49	6.46	6.62	0.34	0.35	51.21
37	0.26	3.30	7.50	0.17	0.39	69.20
42	0.00	0.00	7.79	0.00	0.41	79.62

Table 5. Mixed-mode I/II fracture test results of compacted clay considering support friction.

β ($^\circ$)	M^e	K_I ($\text{kPa}\cdot\text{m}^{0.5}$)	K_{II} ($\text{kPa}\cdot\text{m}^{0.5}$)	K_I/K_{IC}	K_{II}/K_{IC}	T (kPa)
0	1.00	9.41	0.00	1.00	0.00	−24.45
10	0.76	7.52	3.03	0.80	0.32	−7.32
20	0.51	5.29	5.05	0.56	0.54	20.71
30	0.23	2.13	5.65	0.23	0.60	41.57
37	≈ 0.00	≈ 0.00	6.63	≈ 0.00	0.71	60.52
42	−0.22	−2.31	6.51	−0.25	0.69	64.78

The peak load measured in the three-point bending fracture test using fixed support exists in part to resist the friction between the support and the specimen. Therefore, the obtained K_I , K_{II} , and T must show different degrees of the decrease law when the test results are processed by using the previous numerical calibration results (Y_I , Y_{II} , T^*) without considering the support friction.

The fracture phenomena of specimens at different prefabricated crack inclination angles are shown in Figure 15. Under pure mode I loading ($\beta = 0^\circ$), the crack undergoes a self-similar expansion along the direction of the prefabricated crack. As β increases, the crack is deflected along the prefabricated crack direction, and the crack initiation angle θ_0 gradually increases. When β exceeds 30° , the crack initiation angle θ_0 varies little.

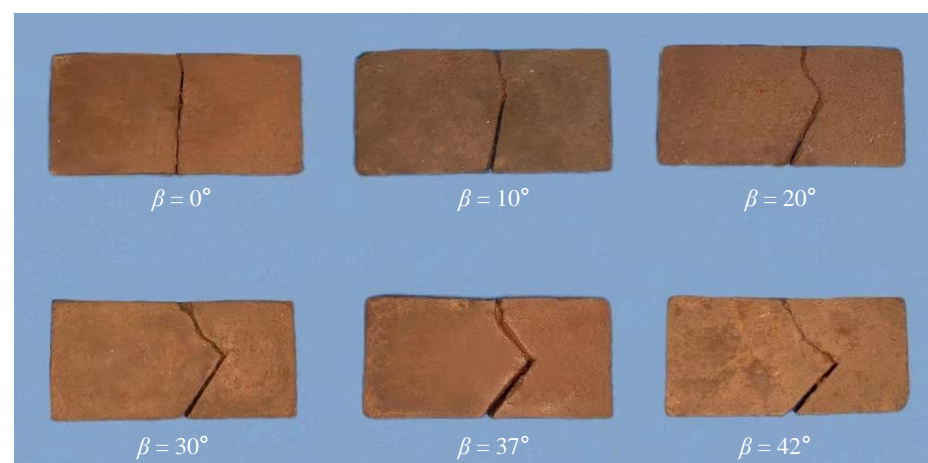


Figure 15. Fractured NDB specimens under different modes.

6. Discussion

The mixed-mode I/II fracture criterion is an important theory for judging whether the crack reaches the propagation condition and the direction of the crack propagation. The most commonly used criteria are the maximum tangential stress (MTS) criterion [43], the minimum strain energy density (MSED) criterion [44] and the maximum energy release rate (MERR) theoretical criterion [45,46]. Studies have shown that these classical criteria have large deviations in predicting the fracture behavior of materials under laboratory conditions [35,47]. Many scholars believe that the non-singular constant term T -stress of the Williams expansion term [19,38,42,47,48] accounts for the failure of conventional fracture mechanics theories to predict experimental results well. The widely adopted GMTS criterion, proposed by Smith et al. [33], considers that the stress field at the crack tip is jointly determined by K_I , K_{II} , and T -stress, the calculation principle of the GMTS criterion is given in Appendix A.

In order to compare the degree of agreement between the theoretical prediction values and the test values considering and not considering the support friction, the crack initiation angle of NDB specimens was theoretically predicted by the GMTS and MTS criteria for both cases considering and not considering the support friction, using the Y_I , Y_{II} , and T^* of NDB specimens and the r_c of compacted clay. According to the tensile strength of compacted clay and the results of K_{IC} testing considering support friction, the r_c of the compacted clay used was calculated to be 7.2 mm using Equation (A8). The prediction result was compared with the experimental results, as shown in Figure 16.

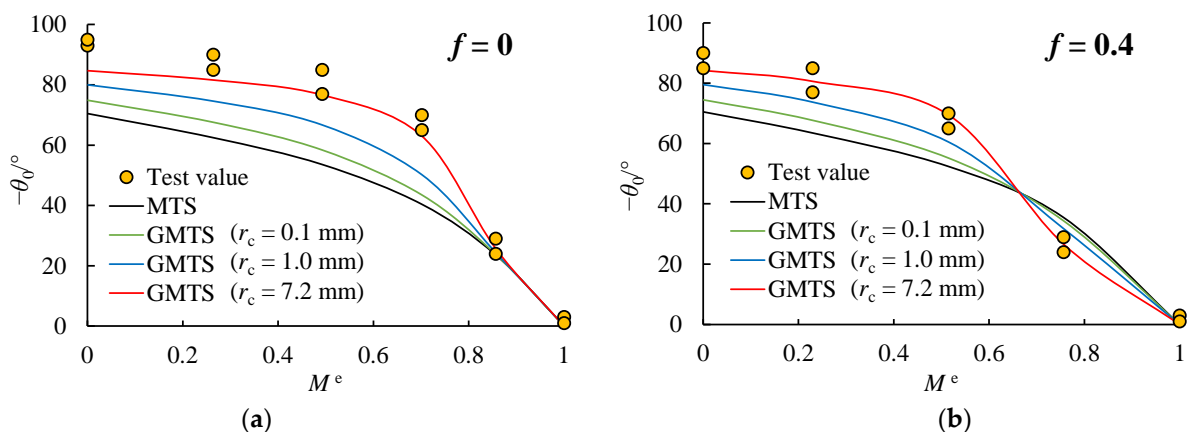


Figure 16. Crack initiation angle direction of the tested NDB specimens and comparison with the MTS and GMTS criteria, (a) without considering support friction, and (b) considering support friction.

The direction of the crack initiation angle was measured from fractured NDB specimens. First, to measure the angle θ_0 for each specimen, the crack front area of the fractured specimen was photographed. A tangent line was drawn from the tip of the crack along the direction of the crack initiation angle. Then, θ_0 was determined by measuring the angle between the original crack line and the tangent line.

From Figure 16, it can be concluded that there is a large deviation between the theoretical prediction curve of the crack initiation angle based on the classical MTS criterion and the experimental results, regardless of whether friction is considered. After the GMTS criterion is adopted, the theoretical prediction curve of the crack initiation angle better agrees with the experimental results.

A comparison of Figure 16a,b shows that the theoretical curve of the GMTS criterion ($r_c = 7.2$ mm) is closer to the experimental data point after considering the support friction. It is worth noting that the critical crack dip angle β_{II} corresponding to pure mode II loading becomes smaller after considering the support friction. Therefore, there is one less set of data points in Figure 16b than in Figure 16a.

Furthermore, the mixed-mode fracture envelope of NDB specimens was plotted based on the GMTS and MTS criteria for both cases considering and not considering the support friction, and was compared with the experimental results, as shown in Figure 17.

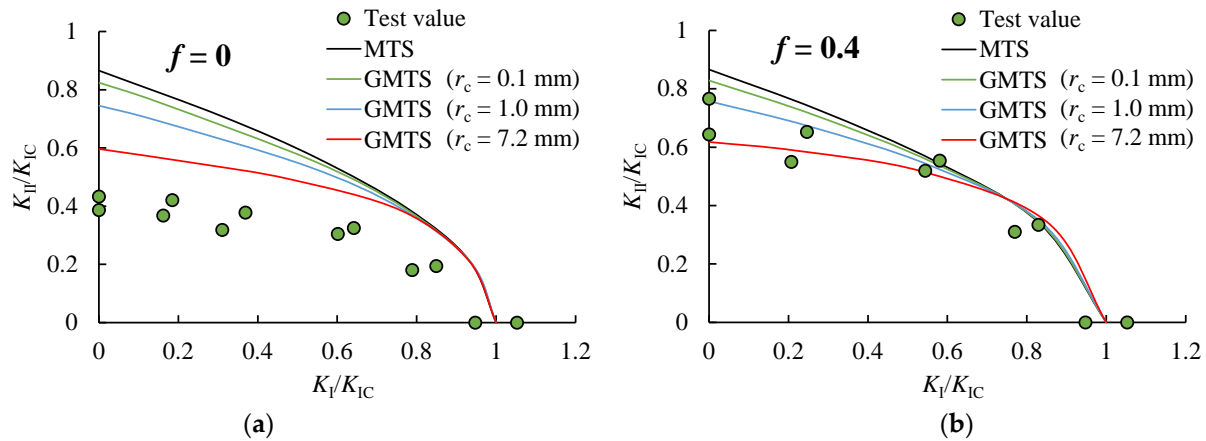


Figure 17. Mixed-mode I/II fracture envelope for the tested NDB specimens and comparison with the MTS and GMTS criteria, (a) without considering support friction, and (b) considering support friction.

Similarly to the pattern in Figure 16, the theoretical curve based on the GMTS criterion is closer to the experimental results than that based on the MTS criterion, regardless of whether friction is considered. In addition, the degree of agreement between the theoretical curve based on the GMTS criterion and the experimental results is significantly improved after considering the support friction.

From Figures 16 and 17, the following conclusions can be drawn: (1) The GMTS criterion can better reveal the mixed-mode fracture failure behavior of compacted clay under indoor laboratory conditions than the MTS criterion, due to the consideration of T -stress. (2) For materials with large r_c values, the support friction has a greater effect on the test results. (3) After considering the support friction, the degree of agreement between the theoretical curves based on the GMTS criterion and the experimental results is significantly improved, which indicates that the effect of support friction on mixed-mode I/II fracture of compacted clay cannot be ignored.

Above all, when the NDB specimen is adopted to conduct the mixed-mode fracture test of compacted clay, the normalized parameters (Y_I , Y_{II} , T^*) considering the support friction should be used to deduce the fracture parameter of the compacted clay NDB specimen in the case of fixed steel support; otherwise, the calculated fracture parameters cannot reflect the real fracture properties of compacted clay.

7. Conclusions

In this paper, the normalized fracture factors (Y_I , Y_{II} and T^*) of the NDB specimen crack were calibrated numerically by considering the crack inclination angle, crack length, support span, and support friction coefficient. Then, the mixed-mode I/II fracture test of compacted clay was performed using NDB specimens. The test results were analyzed by combining the GMTS criteria. The main conclusions are as follows:

1. When the support friction is not considered, as β increases, Y_I decreases gradually, Y_{II} increases first and then decreases, and T^* increases gradually. After considering the support friction, Y_I , Y_{II} , and T^* all tend to decrease, but the trends of $Y_I-\beta$, $Y_{II}-\beta$, and $T^*-\beta$ curves are not affected. When the a/W or S/W is large, the stress concentration at the crack tip of the specimen is greater, resulting in a more significant effect of the support friction coefficient f on Y_I , Y_{II} , and T^* .
2. For the case where pure mode II loading can be achieved originally, increasing the friction coefficient f can effectively reduce the critical inclination angle β_{II} for pure

- mode II loading of crack initiation, which is beneficial for the crack prefabrication in the test. For some cases where pure mode II loading cannot occur originally, pure mode II loading can be achieved by increasing the friction coefficient f .
3. The test data were processed and analyzed using Y_I , Y_{II} , and T^* considering and not considering the support friction. After considering the support friction, the measured fracture parameters all decreased at different degrees, such as K_{IC} decreased by 51%, K_{IIC} decreased by 15%, and the fracture toughness ratio K_{IIC}/K_{IC} increased by 72%, indicating that the support friction increases the proportion of mode II loading at the crack tip.
 4. After considering the support friction, the degree of agreement between the theoretical curves based on the GMTS criterion and the experimental results is significantly improved, which indicates that the effect of support friction on the mixed-mode I/II fracture of compacted clay cannot be ignored.
 5. When the NDB specimen is used to conduct the mixed-mode fracture test of compacted clay, the normalized parameters (Y_I , Y_{II} , and T^*) considering the support friction should be used to deduce the fracture parameter of the compacted clay NDB specimen in the case of fixed support.

Author Contributions: Conceptualization, S.H. and H.D.; Methodology, W.Y. and H.D.; Software, X.L. and X.Z.; Validation, S.H. and W.Y.; Formal analysis, S.H., X.L. and W.Y.; Investigation, S.H., X.L., W.Y. and X.Z.; Resources, S.H., W.Y. and H.D.; Data curation, S.H., X.L. and W.Y.; Writing—original draft preparation, S.H. and X.L.; Writing—review and editing, S.H. and H.D.; Visualization, X.L., X.Z. and H.D.; Supervision, S.H. and H.D.; Funding acquisition, S.H. All authors have read and agreed to the published version of the manuscript.

Funding: This work was funded by the National Natural Science Foundation of China (Grant No. 52109113, 52209121), the Natural Science Foundation of Chongqing, China (cstc2021jcyj-msxmX1114), the Postdoctoral special Funding Project of Chongqing, China (2020921002), and the Ministry of Water Conservancy Embankment Safety and Disease Prevention Engineering Technology Research Center Open Subject Fund Funded Projects (LSDP202101).

Data Availability Statement: The data that support the findings of this study are available within the manuscript.

Conflicts of Interest: The authors declare no conflict of interest.

Nomenclature

NDB	Notched deep beam
CT	Compact tension
SENB	Single-edge notched beam
SCB	Semi-circular bend
ASCB	Asymmetric semi-circular bend
β	Crack inclination angle
a	Crack length
W	Width of specimen
$2W$	Length of specimen
B	Specimen thickness
$2S$	Support span
f	The friction coefficient between the supports and the specimen
K_I	Normalized mode I stress intensity factor
K_{II}	Normalized mode II stress intensity factor
T	T -stress
Y_I	Normalized mode I stress intensity factor
Y_{II}	Normalized mode II stress intensity factor
T^*	Normalized T -stress
β_{II}	Crack inclination angle corresponding to pure mode II loading
M^e	A parameter to describe the relative portions of mode I and mode II loadings at the crack tip

σ_θ Circumferential stress of crack tip
 θ_0 Direction of fracture initiation

Appendix A

In the GMTS criterion, the T -stress was considered in the stress field at the crack tip, thus the tangential stress, σ_θ , at the crack tip is expressed as follows:

$$\sigma_\theta = \frac{1}{\sqrt{2\pi r}} \cos \frac{\theta}{2} \left[K_I \cos^2 \frac{\theta}{2} - \frac{3}{2} K_{II} \sin \theta \right] + T \sin^2 \theta \quad (\text{A1})$$

Similar to conditions in the MTS criterion, the crack initiation conditions in the GMTS criterion are:

$$\frac{\partial \sigma_\theta}{\partial \theta} = 0, \quad \frac{\partial^2 \sigma_\theta}{\partial \theta^2} < 0 \quad (\text{A2})$$

The crack initiation direction, θ_0 , can be determined using the following equation:

$$\frac{\partial \sigma_\theta}{\partial \theta} \Big|_{\theta=\theta_0} = 0 \Rightarrow K_I \sin \theta_0 + K_{II} (3 \cos \theta_0 - 1) - \frac{16T}{3} \sqrt{2\pi r_c} \cos \theta_0 \sin \frac{\theta_0}{2} = 0 \quad (\text{A3})$$

By combining Equations (A1)–(A3), the conditions required for the mixed-mode I/II fracture can be rewritten in terms of mode I fracture toughness K_{IC} :

$$K_{IC} = \cos \frac{\theta_0}{2} \left(K_I \cos^2 \frac{\theta_0}{2} - \frac{3}{2} K_{II} \sin \theta_0 \right) + T \sqrt{2\pi r_c} \sin^2 \theta_0 \quad (\text{A4})$$

By substituting Equations (2)–(4) into Equation (A4), the fracture behavior of the NDB specimen can be predicted theoretically using the normalized fracture parameters Y_I , Y_{II} , and T^* . Then, the crack initiation direction, θ_0 , of the NDB specimen can be determined using the following equation:

$$Y_I \sin \theta_0 + Y_{II} (3 \cos \theta_0 - 1) - \frac{16T^*}{3} \sqrt{\frac{2r_c}{a}} \cos \theta_0 \sin \frac{\theta_0}{2} = 0 \quad (\text{A5})$$

Additionally, the K_I/K_{IC} and K_{II}/K_{IC} ratios of the NDB specimen can be written in terms of Y_I , Y_{II} , and T^* as:

$$\frac{K_I}{K_{IC}} = \frac{1}{\cos \frac{\theta_0}{2} \left[\cos^2 \frac{\theta_0}{2} - \frac{3Y_{II}}{2Y_I} \sin \theta_0 \right] + \sqrt{\frac{2r_c}{a}} \frac{T^*}{Y_I} \sin^2 \theta_0} \quad (\text{A6})$$

$$\frac{K_{II}}{K_{IC}} = \frac{1}{\cos \frac{\theta_0}{2} \left[\frac{Y_I}{Y_{II}} \cos^2 \frac{\theta_0}{2} - \frac{3}{2} \sin \theta_0 \right] + \sqrt{\frac{2r_c}{a}} \frac{T^*}{Y_{II}} \sin^2 \theta_0} \quad (\text{A7})$$

In applying the GMTS guidelines, the critical distance from the crack tip (r_c) is another necessary parameter. According to the maximum principal stress model introduced by Schmidt [49], r_c can be calculated by:

$$r_c = \frac{1}{2\pi} \left(\frac{K_{IC}}{\sigma_t} \right)^2 \quad (\text{A8})$$

where K_{IC} and σ_t are the mode I fracture toughness and tensile strength of the material, respectively.

References

1. Ji, E.; Fu, Z.; Chen, S.; Zhu, J.; Geng, Z. Numerical Simulation of Hydraulic Fracturing in Earth and Rockfill Dam Using Extended Finite Element Method. *Adv. Civ. Eng.* **2018**, *2018*, 1782686. [[CrossRef](#)]
2. Zhang, H.; Jing, Y.; Chen, J.; Gao, Z.; Xu, Y. Characteristics and causes of crest cracking on a high core-wall rockfill dam: A case study. *Eng. Geol.* **2022**, *297*, 106488. [[CrossRef](#)]
3. Liu, Y.; Zheng, D.; Cao, E.; Wu, X.; Chen, Z. Cracking risk analysis of face slabs in concrete face rockfill dams during the operation period. *Structures* **2022**, *40*, 621–632. [[CrossRef](#)]
4. Qu, Y.; Zou, D.; Kong, X.; Yu, X.; Chen, K. Seismic cracking evolution for anti-seepage face slabs in concrete faced rockfill dams based on cohesive zone model in explicit SBFEM-FEM frame. *Soil Dyn. Earthq. Eng.* **2020**, *133*, 106106. [[CrossRef](#)]
5. Skempton, A.W.; Schuster, R.L.; Petley, D.J. Joints and Fissures in The London Clay at Wraybury and Edgware. *Géotechnique* **1970**, *20*, 208–209. [[CrossRef](#)]
6. Lakshminantha, M.R.; Prat, P.C.; Ledesma, A. Experimental evidence of size effect in soil cracking. *Can. Geotech. J.* **2012**, *49*, 264–284. [[CrossRef](#)]
7. Lee, F.H.; Lo, K.W.; Lee, S.L. Tension Crack Development in Soils. *J. Geotech. Eng.* **1988**, *114*, 915–929. [[CrossRef](#)]
8. *ASTM Standard E399-12*; Standard Test Method for Linear-Elastic Plane-Strain Fracture Toughness K_{IC} of Metallic Materials. Annual Book of ASTM Standards. ASTM International: West Conshohocken, PA, USA, 2013.
9. Zhang, Z.G.; Ding, J.S. Studies on the fracture toughness K_{IC} of cohesive soil. *Rock Soil Mech.* **1993**, *14*, 47–52. (In Chinese) [[CrossRef](#)]
10. Wang, J.; Huang, S.; Hu, J. Limit of crack depth in K_{IC} testing for a clay. *Eng. Fract. Mech.* **2016**, *164*, 19–23. [[CrossRef](#)]
11. Lenci, S.; Clementi, F.; Sadowski, T. Experimental determination of the fracture properties of unfired dry earth. *Eng. Fract. Mech.* **2012**, *87*, 62–72. [[CrossRef](#)]
12. Amarasiri, A.L.; Costa, S.; Kodikara, J.K. Determination of cohesive properties for mode I fracture from compacted clay beams. *Can. Geotech. J.* **2011**, *48*, 1163–1173. [[CrossRef](#)]
13. Wang, J.; Zhu, J.; Chiu, C.F.; Zhang, H. Experimental study on fracture toughness and tensile strength of a clay. *Eng. Geol.* **2007**, *94*, 65–75. [[CrossRef](#)]
14. Aluko, O.B.; Chandler, H.W. A Fracture Strength Parameter for Brittle Agricultural Soils. *Biosyst. Eng.* **2006**, *93*, 245–252. [[CrossRef](#)]
15. Qiao, L.; Liu, J.; Li, X.; Li, Q.; Xie, J. Experimental study on mode I fracture characteristics of compacted bentonite clay. *Eng. Fract. Mech.* **2023**, *285*, 109294. [[CrossRef](#)]
16. Wang, J.; Huang, S.; Guo, W.; Qiu, Z.; Kang, K. Experimental study on fracture toughness of a compacted clay using semi-circular bend specimen. *Eng. Fract. Mech.* **2020**, *224*, 106814. [[CrossRef](#)]
17. Kuruppu, M.D.; Obara, Y.; Ayatollahi, M.R.; Chong, K.P.; Funatsu, T. ISRM-Suggested Method for Determining the Mode I Static Fracture Toughness Using Semi-Circular Bend Specimen. *Rock Mech. Rock Eng.* **2014**, *47*, 267–274. [[CrossRef](#)]
18. Wang, J.; Zhu, J.; Chiu, C.F.; Chai, H. Experimental Study on Fracture Behavior of a Silty Clay. *Geotech. Test. J.* **2007**, *30*, 100715. [[CrossRef](#)]
19. Aliha, M.R.M.; Jafari Haghghatpour, P.; Taviana, A. Application of asymmetric semi-circular bend test for determining mixed mode I + II fracture toughness of compacted soil material. *Eng. Fract. Mech.* **2022**, *262*, 108268. [[CrossRef](#)]
20. Negru, R.; Marsavina, L.; Filipescu, H.; Pasca, N. Investigation of Mixed Mode I/II Brittle Fracture Using ASCB Specimen. *Int. J. Fract.* **2013**, *181*, 155–161. [[CrossRef](#)]
21. Vesga, L.F.; Vallejo, L.E.; Lobo-Guerrero, S. DEM analysis of the crack propagation in brittle clays under uniaxial compression tests. *Int. J. Numer. Anal. Met.* **2008**, *32*, 1405–1415. [[CrossRef](#)]
22. Vallejo, L.E. The brittle and ductile behavior of clay samples containing a crack under mixed mode loading. *Appl. Fract. Mec.* **1988**, *10*, 73–78. [[CrossRef](#)]
23. Luo, Y.; Ren, L.; Xie, L.Z.; Ai, T.; He, B. Fracture Behavior Investigation of a Typical Sandstone Under Mixed-Mode I/II Loading Using the Notched Deep Beam Bending Method. *Rock Mech. Rock Eng.* **2017**, *50*, 1987–2005. [[CrossRef](#)]
24. Mousavi, S.S.; Aliha, M.R.M.; Imani, D.M. On the use of edge cracked short bend beam specimen for PMMA fracture toughness testing under mixed-mode I/II. *Polym. Test.* **2020**, *81*, 106199. [[CrossRef](#)]
25. Bahrami, B.; Ayatollahi, M.R.; Mirzaei, A.M.; Yahya, M.Y. Support Type Influence on Rock Fracture Toughness Measurement Using Semi-circular Bending Specimen. *Rock Mech. Rock Eng.* **2020**, *53*, 2175–2183. [[CrossRef](#)]
26. Bahrami, B.; Ayatollahi, M.R.; Sedighi, I.; Yazid Yahya, M. An insight into mode II fracture toughness testing using SCB specimen. *Fatigue Fract. Eng. Mater. Struct.* **2019**, *42*, 1991–1999. [[CrossRef](#)]
27. Xie, Q.; Zeng, Y.; Li, S.; Liu, X.; Du, K. The influence of friction on the determination of rock fracture toughness. *Sci. Rep.* **2022**, *12*, 7332. [[CrossRef](#)]
28. Pirmohammad, S.; Abdi, M.; Ayatollahi, M.R. Effect of support type on the fracture toughness and energy of asphalt concrete at different temperature conditions. *Eng. Fract. Mech.* **2021**, *254*, 107921. [[CrossRef](#)]
29. Pirmohammad, S.; Abdi, M.; Ayatollahi, M.R. Mode II fracture tests on asphalt concrete at different temperatures using semi-circular bend specimen loaded by various types of supports. *Appl. Fract. Mec.* **2021**, *116*, 103089. [[CrossRef](#)]
30. Bakhshizadeh, M.; Pirmohammad, S.; Ayatollahi, M.R. Effect of friction at the supports of semi-circular bending tests on fracture mode of loading. *Appl. Fract. Mec.* **2022**, *118*, 103265. [[CrossRef](#)]

31. Ayatollahi, M.R.; Bahrami, B.; Mirzaei, A.M.; Yazid Yahya, M. Effects of support friction on mode I stress intensity factor and fracture toughness in SENB testing. *Appl. Fract. Mec.* **2019**, *103*, 102288. [[CrossRef](#)]
32. Sedighi, I.; Ayatollahi, M.R.; Bahrami, B. A statistical approach on the support type effect on mode I fracture toughness determined using semi-circular bend (SCB) specimen. *Eng. Fract. Mech.* **2020**, *226*, 106891. [[CrossRef](#)]
33. Smith, D.J.; Ayatollahi, M.R.; Pavier, M.J. The role of T-stress in brittle fracture for linear elastic materials under mixed-mode loading. *Fatigue Fract. Eng. Mater. Struct.* **2001**, *24*, 137–150. [[CrossRef](#)]
34. Irwin, G. Analysis of Stresses and Strains Near End of a Crack Traversing a Plate. *J. Appl. Mech.* **1957**, *24*, 361–364. [[CrossRef](#)]
35. Wei, M.; Dai, F.; Xu, N.; Liu, Y.; Zhao, T. Fracture prediction of rocks under mode I and mode II loading using the generalized maximum tangential strain criterion. *Eng. Fract. Mech.* **2017**, *186*, 21–38. [[CrossRef](#)]
36. Aliha, M.R.M.; Saghafi, H. The effects of thickness and Poisson's ratio on 3D mixed-mode fracture. *Eng. Fract. Mech.* **2013**, *98*, 15–28. [[CrossRef](#)]
37. Huang, X.; Liu, Y.; Dai, Y. Characteristics and effects of T-stresses in central-cracked unstiffened and stiffened plates under mode I loading. *Eng. Fract. Mech.* **2018**, *188*, 393–415. [[CrossRef](#)]
38. Ayatollahi, M.R.; Rashidi Moghaddam, M.; Berto, F. T-stress effects on fatigue crack growth—Theory and experiment. *Eng. Fract. Mech.* **2018**, *187*, 103–114. [[CrossRef](#)]
39. Saghafi, H.; Monemian, S. A New Fracture Toughness Test Covering Mixed-Mode Conditions and Positive and Negative T-Stresses. *Int. J. Fract.* **2010**, *165*, 135–138. [[CrossRef](#)]
40. Smith, D.J.; Ayatollahi, M.R.; Pavier, M.J. On the consequences of T-stress in elastic brittle fracture. *Proc. R. Soc. A Math. Phys. Eng. Sci.* **2006**, *462*, 2415–2437. [[CrossRef](#)]
41. Wang, J.; Lv, C.; Huang, S.; Qiu, Z. Size effect on fracture behavior of quasi-brittle materials during uniaxial compression tests. *Arch. Appl. Mech.* **2023**, *93*, 3171–3188. [[CrossRef](#)]
42. Fan, Y.; Zhu, Z.; Zhao, Y.; Zhou, L.; Qiu, H.; Niu, C. Analytical solution of T-stresses for an inclined crack in compression. *Int. J. Rock Mech. Min.* **2021**, *138*, 104433. [[CrossRef](#)]
43. Erdogan, F.; Sih, G.C. On the Crack Extension in Plates Under Plane Loading and Transverse Shear. *J. Basic Eng.* **1963**, *85*, 519–525. [[CrossRef](#)]
44. Sih, G.C. Strain-energy-density factor applied to mixed mode crack problems. *Int. J. Fract.* **1974**, *10*, 305–321. [[CrossRef](#)]
45. Nuismer, R.J. An energy release rate criterion for mixed mode fracture. *Int. J. Fract.* **1975**, *11*, 245–250. [[CrossRef](#)]
46. Chen, H.; Xing, H.; Imtiaz, H.; Liu, B. How to obtain a more accurate maximum energy release rate for mixed mode fracture. *Forces Mech.* **2022**, *7*, 100077. [[CrossRef](#)]
47. Hou, C.; Jin, X.; Fan, X.; Xu, R.; Wang, Z. A generalized maximum energy release rate criterion for mixed mode fracture analysis of brittle and quasi-brittle materials. *Appl. Fract. Mec.* **2019**, *100*, 78–85. [[CrossRef](#)]
48. Williams, J.G.; Ewing, P.D. Fracture under complex stress—The angled crack problem. *Int. J. Fract. Mech.* **1972**, *8*, 441–446. [[CrossRef](#)]
49. Schmidt, R. A microcrack model and its significance to hydraulic fracturing and fracture toughness testing. In Proceedings of the 21st U.S. Symposium on Rock Mechanics (USRMS), Rolla, MI, USA, 27–30 May 1980; pp. 581–590. [[CrossRef](#)]

Disclaimer/Publisher's Note: The statements, opinions and data contained in all publications are solely those of the individual author(s) and contributor(s) and not of MDPI and/or the editor(s). MDPI and/or the editor(s) disclaim responsibility for any injury to people or property resulting from any ideas, methods, instructions or products referred to in the content.